Imjai, T., Setkit, M., Figueiredo, F.P., **Garcia, R.**, Sae-Long, W. and Limkatanyu, S., 2022. Experimental and numerical investigation on low-strength RC beams strengthened with side or bottom near surface mounted FRP rods. *Struct. Infrastruct. Eng.*, pp.1-16. https://doi.org/10.1080/15732479.2022.2045613

Experimental and numerical investigation on low-strength RC beams strengthened with side or bottom Near Surface Mounted FRP rods

Thanongsak Imjai[a,*], Monthian Setkit[a], Fabio P. Figueiredo[b], Reyes Garcia[c], Worathep Sae-Long[d] and Suchart Limkatanyu[e]

[a] *School of Engineering and Technology, and Center of Excellence in Sustainable Disaster Management, Walailak University, Nakhonsithammarat, Thailand 80161; thanongsak.im@wu.ac.th, smonthia@wu.ac.th*

[b] *School of Engineering, University of Minho, Guimarães 4800-058, Portugal; f.figueiredo@civil.uminho.pt*

[c] *Civil Engineering Stream, School of Engineering, The University of Warwick, Coventry, UK CV4 7AL; reyes.garcia@warwick.ac.uk*

[d] *Department of Civil Engineering, School of Engineering, University of Phayao, Phayao, Thailand 56000; s.worathep@yahoo.com*

[e] *Department of Civil Engineering, Prince of Songkla University, Hadyai, Songkhla, Thailand 90110; suchart.l@psu.ac.th*

** Correspondence: thanongsak.im@wu.ac.th; Tel.: +66 (0) 7567 2378*

Imjai, T., Setkit, M., Figueiredo, F.P., **Garcia, R.**, Sae-Long, W. and Limkatanyu, S., 2022. Experimental and numerical investigation on low-strength RC beams strengthened with side or bottom near surface mounted FRP rods. *Struct. Infrastruct. Eng.*, pp.1-16. https://doi.org/10.1080/15732479.2022.2045613

Experimental and numerical investigation on low-strength concrete beams strengthened with side or bottom Near Surface Mounted FRP rods

This article examines experimentally and numerically the flexural performance of low-strength reinforced concrete (RC) beams strengthened using near-surface mounted (NSM) carbon fibre reinforced polymer (CFRP) rods. Five RC rectangular beams were tested in four-point bending until failure. Four of these beams were strengthened using Bottom NSM (BNSM) or Side NSM (SNSM) rods. The results are discussed in terms of observed damage, load capacity, and midspan deflection. It is shown that the SNSM strengthening solution enhanced the cracking load of the beams by up to 19%. Likewise, the yield and ultimate load-carrying capacities of the strengthened beams increased by up to 31% and 64%, respectively. It is also shown that moment-curvature and FE approaches predict well the deflections of the strengthened RC beams within 20% and 10% of accuracy at failure. The results from nonlinear Finite Element (FE) analyses showed a better agreement with the experimental results up to failure (within a 10% of accuracy). For the beams presented in this study, the crack widths calculated by Eurocode 2 match reasonably well the measured values.

Keywords: ***Near surface mounted; Low strength concrete; FRP; Serviceability, Strengthening; Finite element analysis.***

1. Introduction

Many existing reinforced concrete (RC) structures need to be strengthened due to issues such as lack of maintenance, accidental damage, the need for extending their service life or an update of design guidelines. In rural areas of developing countries, the use of hand-mixed low-strength concrete is another issue that increases the vulnerability of such existing structures. Several solutions have been proposed to strengthen low-strength RC members, such as section overlays or concrete patching. However, such methods are often time-consuming and usually increase the overall weight and size of the existing members.

Previous research has shown that the use of Fibre Reinforcement Polymers (FRPs) strengthening was successful at restoring the capacity of low-strength RC elements (Al-Mahmoud et al., 2009; Bilotta et al., 2015; Gudonis et al., 2014; Nanni, 2003; Parvin & Shah, 2016; Sharaky et al., 2014; Siddika et al., 2019; Siddika, et al., 2020; Spadea, et al., 2015). FRPs have been increasingly used in the strengthening of RC structures due to their ease of installation, lightweight, high strength to weight ratio, and excellent durability (Gudonis et al., 2014; Kim, 2019; Nanni, 2003; Osman et al., 2017; Setunge & Nezamian, 2004; Siddika et al., 2019, 2020; Teng et al., 2012). Previous research also indicates that the use of externally bonded FRP reinforcement (see Figure 1(a)) can substantially increase the flexural capacity of RC beams in service and ultimate conditions (Barros et al., 2007; Nanni, 2003; Osman et al., 2017; Teng et al., 2012; Kim & Andrawes, 2017).

Current design guidelines for flexural strengthening of beams with FRP assume a full composite action between the FRP and the concrete (fib Task Group 5.1, 2019; DAfStb Heft 595, 2013; ACI 440.1R, 2017). As a result, potential failures such as i) end-plate debonding at the end anchorage and ii) debonding along the FRP, must be always avoided (Bilotta et al., 2015; Sharaky et al., 2014). These failures can not only prevent an FRP-strengthened element from reaching its theoretical ultimate capacity, but it can also limit its ductility (Imjai & Garcia, 2017; Imjai et al., 2017; Oehlers, 2001; Pešić & Pilakoutas, 2003; Spadea et al., 2015; Yao et al., 2005; Oller et al., 2011; Zhang & Smith, 2017; Zhou et al., 2017).

One of the main drawbacks of externally bonded FRP reinforcement is its tendency to debond from the concrete substrate. Several models and design guidelines exist to predict the bond behaviour of FRP systems, although they are still unable to give accurate predictions (Bilotta et al., 2013; Oehlers, 2001; Pešić & Pilakoutas, 2003; Smith

& Teng, 2002a, 2002b; Teng et al., 2006; Abid & Al-lami, 2018;). The large scatter in results can be attributed to a lack of understanding of the development of bond stress along the FRP-concrete interface, especially at the end section where high interfacial stresses are mobilised (Bilotta et al., 2013; Imjai et al., 2017; Oehlers, 1992; Sharaky et al., 2014; Smith & Teng, 2002a; Spadea et al., 2015; Zhang & Smith, 2017). To improve the bond strength of FRP reinforcement, the use of Near-Surface Mounted (NSM) FRPs was proposed as an alternative to strengthen flexural-dominated RC structures (Al-Mahmoud et al., 2009; Parretti & Nanni, 2004; Sena-Cruz et al., 2016; Al-Saadi et al, 2019; Gravina et al. 2018; Laraba et al. 2014).

The NSM technique consists of FRP strips or rods embedded in pre-cut grooves made on the concrete surface and filled/bonded with epoxy adhesive (Oehlers, 1992; Parretti & Nanni, 2004; Sena-Cruz et al., 2016), as shown schematically in Figure 1(b). Results from numerous studies indicate that the flexural capacity of NSM FRP-strengthened specimens increases between 30-70% over unstrengthened specimens (De Lorenzis & Teng, 2007; Gopinath et al., 2016; Hosen et al., 2015; Pachalla & Prakash, 2017; Parvin & Shah, 2016; Rezazadeh et al., 2016; Sharaky et al., 2014, 2014; Shukri et al., 2016; Siddika et al., 2019; Szabó & Balázs, 2007; Zhang et al., 2017). NSM FRP systems are usually applied at the soffit of RC beams and slabs (Figure 1(b)), which implies that such elements are wide enough to accommodate the necessary edge clearance and clear spacing between adjacent NSM grooves (Al-Mahmoud et al., 2009; Oehlers, 1992; Parretti & Nanni, 2004; Sena-Cruz et al., 2016). However, in many existing structures, beams and slabs hold suspended ceilings, air ducts/extractors, and electrical wiring at their soffit, as shown in Figure 1(c). This in turn hinders the cutting of the grooves necessary to install the NSM FRP reinforcement. Consequently, it is necessary to investigate alternative strengthening locations (other than the soffit) to make NSM

systems more adaptable and versatile.

To date, only a few studies have investigated the performance of side NSM FRP strengthening as that shown in Figure 1(d) (Hosen et al. 2017; Hosen et al., 2018; Hosen et al., 2015; Imjai et al., 2020; Sabau et al., 2018; Sharaky et al., 2017; Shukri et al., 2016), and none of these studies has reported results from low-strength RC elements. Moreover, as serviceability (e.g. deflections and crack widths) often control the design of NSM FRP-strengthened elements, further experimental and numerical research is necessary to assess the accuracy of current design guidelines at predicting the behaviour of these elements.

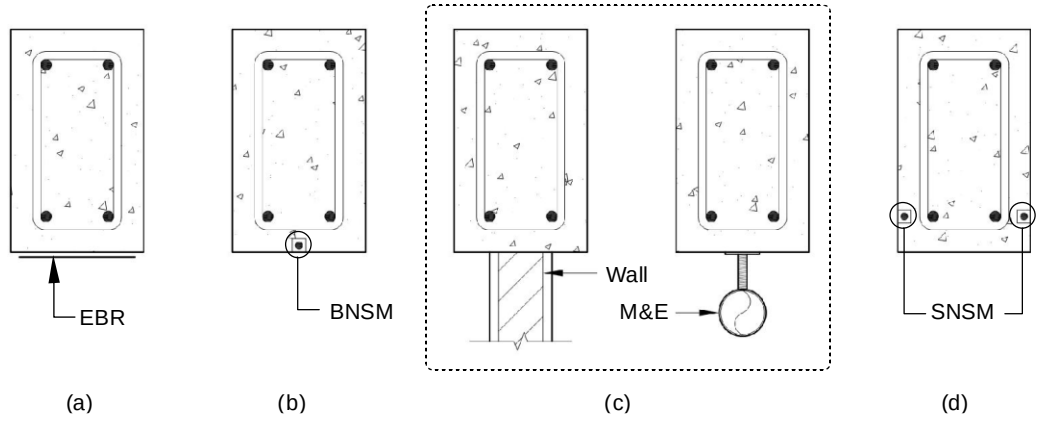

Figure 1. Strengthening configurations for concrete elements (a) conventional externally bonded FRP reinforcement; (b) bottom near-surface mounted (BNSM), (c) potential obstacles for BNSM installation, and (d) side near-surfaced mounted (SNSM).

This article investigates experimentally and numerically the flexural behaviour of FRP-strengthened RC beams with Side and Bottom NSM FRP reinforcement. Side NSM (SNSM) is used to overcome some of the practical hindrances of Bottom NSM (BNSM). The results are discussed in terms of observed damage, load capacity and deflections. The effectiveness of nonlinear finite element modelling and sectional analysis at predicting the flexural behaviour and deflections of the strengthened beams is also discussed. This study contributes towards a better understanding of the effects of flexural NSM FRP

strengthening on low-strength RC structures, which in turn is relevant to improve the calculation of deflections in such elements.

2. Experimental programme

The experimental programme involved the preparation, casting, strengthening, and testing of five low-strength RC beams. Three of these five beams (control TB1, and NSM FRP-strengthened beams TB3 and TB4) were part of a previous study (Imjai et al., 2020) aimed at investigating the effectiveness of an innovative strengthening technique that uses post-tensioned metal straps on pre-damaged RC beams. In the present study, two new NSM FRP-strengthened beams were tested (TB2 and TB5). All specimens were tested in four-point bending up to failure to examine the serviceability and ultimate performance of the Bottom-NSM (BNSM) and Side-NSM (SNSM) strengthening solutions.

2.1. Beams geometry and reinforcement

All beams had a cross-section of 150×250 mm with internal steel reinforcement designed according to ACI 318 (2019). Two ϕ12 mm steel bars (f_y= 392 MPa) were used as flexural bottom reinforcement in all specimens, thus leading to a flexural reinforcement ratio ρ_f =0.73%. Such reinforcement ratio was higher than the minimum required by the ACI code, and 59.3% of the maximum reinforcement ratio required by the same code. The top reinforcement in the compression zone (outside the midspan) consisted of two ϕ9 mm steel bars (f_y= 235 MPa), which were also used to hold vertical steel stirrups. Shear failure was prevented by adding two-legged steel stirrups of ϕ9 mm at a spacing of 100 mm (ρ_w= 0.84%).

Figure 2 shows the general geometry and reinforcement of the beam specimens included in this study. Beam TB1 (Figure 2(a)) was a control specimen. Beam TB2

(Figure 2(b)) was strengthened with one NSM CFRP rod inserted into a pre-cut groove at the beam soffit (BNSM). Beams TB3 to TB5 (Figure 2(c)-(d)) had different amounts and configurations of NSM CFRP reinforcement. It should be noted that the NSM CFRP rods in beam TB4 are placed above the neutral axis and as such these rods are not expected to increase the flexural capacity of the beam. However, beam TB4 replicates an inverted RC beam with limited lateral access due to the possible presence of a slab. This type of beams is very common in existing buildings of many developing countries, including Thailand. Whilst not ideal, in this case the CFRP rods could only be installed in the compression zone of the beam even if this implies somehow damaging the compression zone of the beam. Table 1 summarises the details of the beam specimens considered in this study.

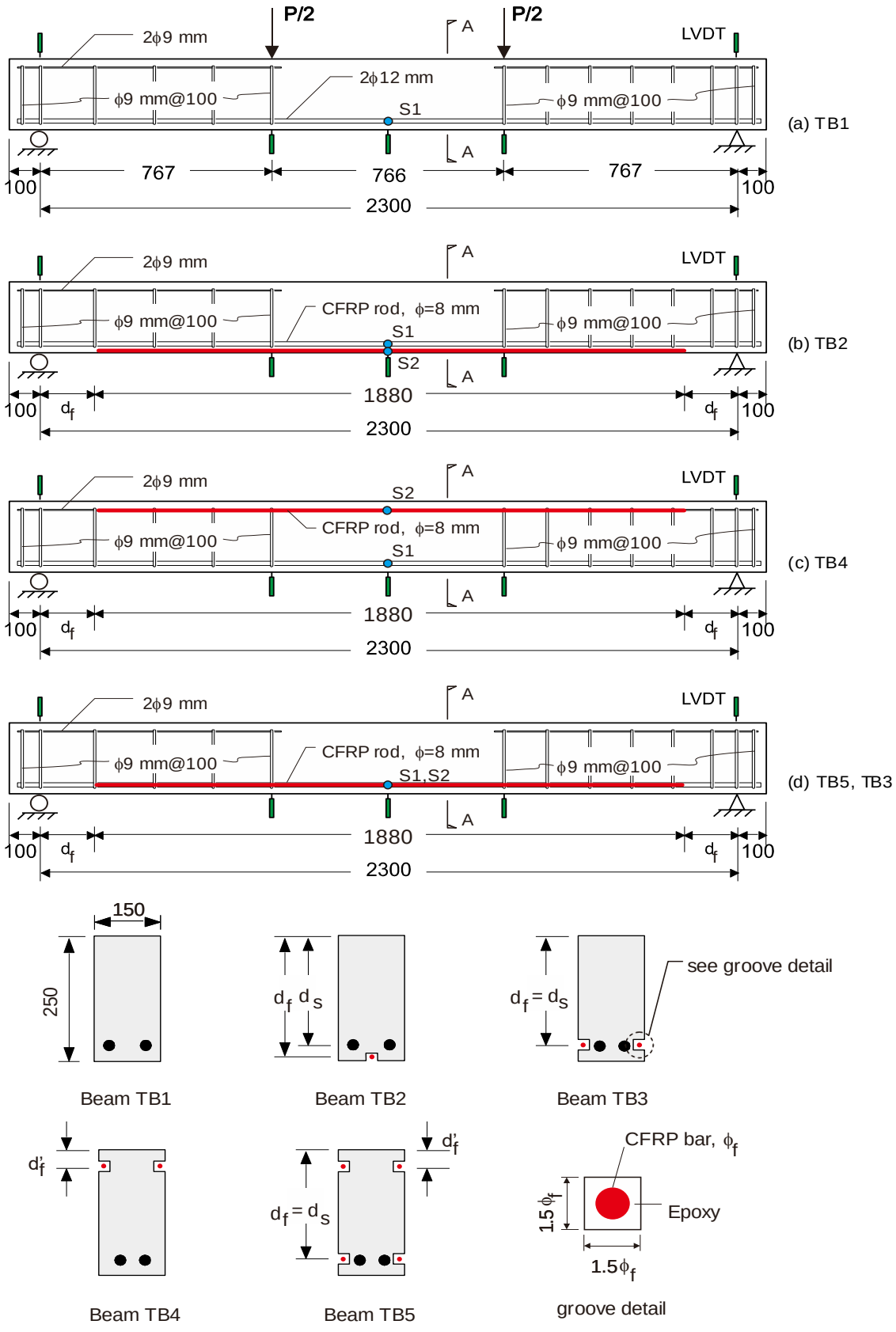

(e) Bottom and Side NSM installation at section A-A

Figure 2. Geometry, internal reinforcement and NSM FRP strengthening configurations of beams TB1 to TB5 (units: mm).

Table 1. Details of RC beams TB1 to TB5.

ID	Configuration	No. of NSM CFRP rods	d_s (mm)	d_f (mm)	d'_f (mm)
TB1[a]	Control	-	210	-	-
TB2	Bottom NSM FRP (tension side)	1-ϕ8 (BNSM)	210	244	-
TB3 (B3-SNSM[a])	Side NSM FRP (tension side)	2-ϕ8 (SNSM)	210	210	-
TB4 (B2-SNSM[a])	Side NSM FRP (compression side)	2-ϕ8 (SNSM)	210	-	40
TB5	Side NSM FRP (compression side) + Side NSM FRP (tension side)	2-ϕ8 (SNSM) 2-ϕ8 (SNSM)	210	210	40

[a] The IDs of beams TB1, TB3 and TB4 were different in Imjai et al. (2020) and they are included here to avoid confusion.

2.2. Concrete properties

The beams were cast using low-strength concrete that reflects the quality of concrete used in rural areas of Thailand. The mix design is shown in Table 2. The reported average compressive strength of concrete (f_c=15.3 MPa) was obtained from 150 mm cylinders according to BS EN 12390-3 (1983a). The average indirect tensile splitting strength (f_t=1.4 MPa) was determined from tests on 150×300 mm cylinders, according to BS EN 12390-6 (1983b). The average flexural strength (f_b=1.9 MPa) was obtained from 100×100×500 mm prisms tested in four-point bending according to BS EN 12390-5 (1983c). Table 3 lists the mean mechanical properties and standard deviations of the concrete used to cast the beams.

Table 2. Concrete mix proportion.

Mix proportion (kg/m^3)				w/c ratio	Slump (mm)
Cement	Coarse aggregate	Fine aggregate	Water + Plasticizer		
250	1120	757	200	0.77	75

Table 3. Mechanical properties of concrete.

Statistical values	Cylinder compressive strength (f_c)	Cube compressive strength ($f_{c,cube}$)	Tensile strength (f_t)	Modulus of rupture (f_b)
Mean (MPa)	15.3	17.1	1.4	1.9
Std. Dev. (MPa)	2.3	3.5	0.5	0.2
No. of samples	6	6	6	6

2.3. Concrete beams strengthened with BNSM and SNSM FRP rods

An NSM FRP technique was used to strengthen beams TB2 to TB5. The cutting of the grooves and installation were carried out according to ACI 440.2R (2017). The grooves were first cut using a diamond blade with dimension 12×12 mm compliant with ACI 440.2R. The grooves were subsequently cleaned with high-pressurised air and acetone.

A two-part epoxy adhesive (Hernandez & Orlandi, 2016) was used to bond the CFRP rods into the groove (Figure 3(a)), as proposed in past studies (Hosen et al., 2017, 2015; Imjai et al., 2020). Sand-coated Carbon FRP (CFRP) rods of size ϕ8 mm were used, with a fibre volume fraction of 68% (Figure 3(b)). The tensile strength of the rods (f_{fu}) was 2400 MPa, and the modulus of elasticity (E_f) was 120 GPa, with an elongation at rupture (ε_{fu}) of 1.5%. To insert the 1880 mm-long CFRP rods, the grooves were fully filled in with epoxy adhesives, as shown in Figure 3(c). After inserting the rods into the grooves (Figure 3(d)), the excess epoxy adhesive was removed. For the SNSM strengthening solution, longitudinal CFRP rods were inserted into the grooves on both sides of the beam, at 40 mm below its top/bottom faces (see TB3, TB4 and TB5 in Figure 2(e)). The BNSM strengthening solution consisted of a single CFRP rod inserted into a groove at the beam soffit (TB2). In this study, the anchorage length of the NSM reinforcement was not an experimental parameter. Accordingly, the CFRP rods were cut at a distance d_f=210 mm

away from the support (Figure 2(b) to (d)). This is justified because, in real practical applications, it is impossible to extend the groove much closer to the support as the diamond blade tool and operator need some space to work.

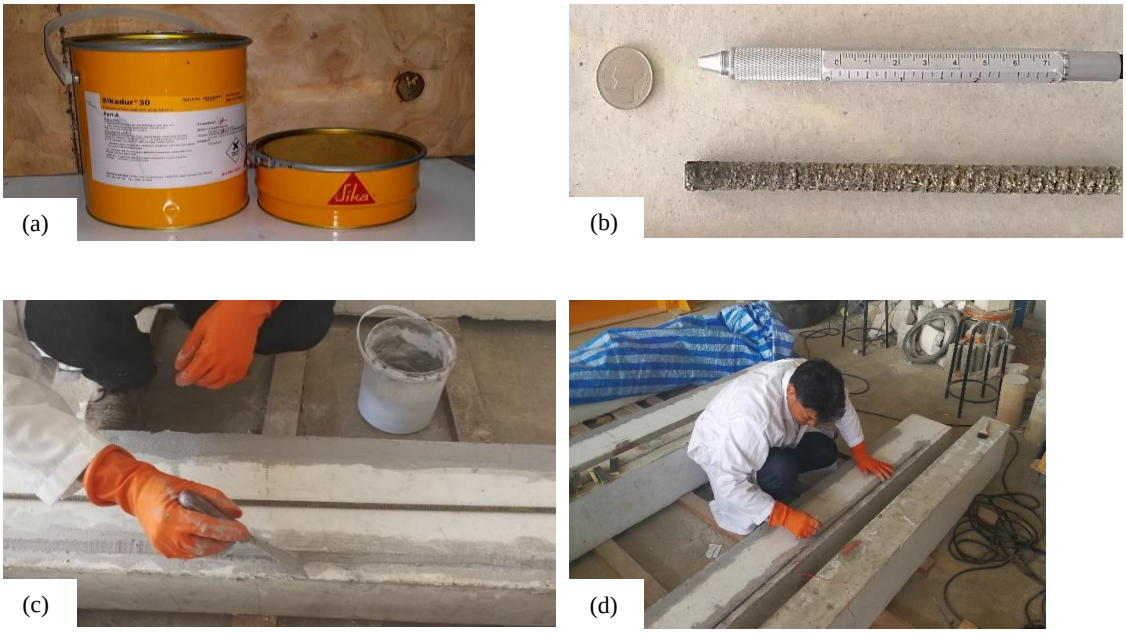

Figure 3. Installation of NSM CFRP rod (a) CFRP rod, (b) two-part adhesive epoxy resin, (c) filling of epoxy adhesive before installation of CFRP rod (d) inserting CFRP rod into a groove.

2.4. Test setup and instrumentation

All the simply supported specimens were tested in four-point bending, with the setup shown in Figure 4. The free span was 2300 mm, whereas the shear span was 767 mm. To promote a flexural-dominated behaviour, the shear span to effective depth ratio of the beams was 3.65 (effective depth = 210 mm). Adequate shear reinforcement prevented shear failures at the shear span. The loading was applied using a 1,000 kN actuator in displacement control mode at a loading rate of 1.0 mm/min. The deflections at the constant moment zone were measured using three linear variable displacement transducers (LVDTs). Two additional LVDTs were also placed on the beams' top face (above the supports) to calculate net deflections. Strain gauges were attached to the

flexural reinforcement within the midspan of each beam. Strain gauge S1 measured the strain in the longitudinal steel bar, whereas gauge S2 measured the strains in the CFRP rod (see Figure 2(a)-(d)).

At each loading step, cracks were marked and the width of selected cracks was measured using a handheld micrometre (accuracy = 0.002 mm) at approximately every 5.0 kN. Particular attention was paid to measuring and recording of the width and length of the cracks at the constant moment zone of the NSM FRP-strengthened beams. The beams were then loaded up to a load P_y that produced yielding of the flexural reinforcement, i.e. once the strain gauge S1 readings were approximately 0.002-0.0025. Eventually, all beams were tested up to failure (TB2-TB5), or up to a deflection where the load started to drop (TB1), which was defined as the 'failure' load.

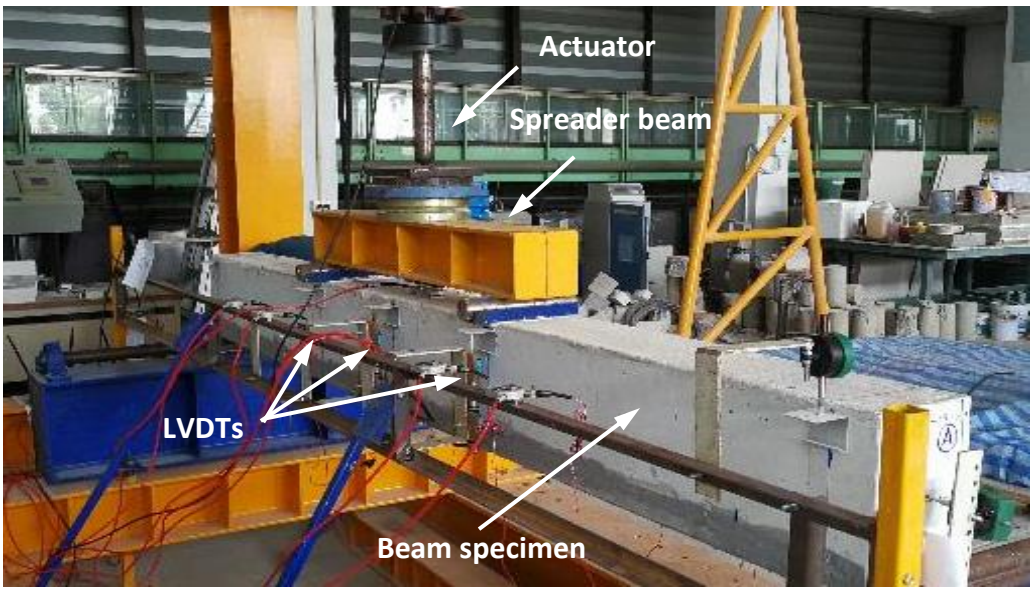

Figure 4. Typical setup and instrumentation used for tested beams.

3. Test results and discussion

3.1. Failure mode and ultimate performance

Figure 5 compares the load-midspan deflection curves of the five beams. The

maximum recorded load was considered the ultimate capacity (P_u), whereas the load at which the test was terminated was considered the failure load (P_f). The corresponding moment (M) of the beams was calculated as M=P/2·a, where a is the shear span (a=767 mm). Initially, small flexural cracks formed within the midspan and shear span region, and existing cracks became wider and visible to the naked eye as the load increased. As shown in Figure 5, all the specimens had a linear response until the first concrete cracking occurs (at P_{cr}). The difference in flexural stiffness after the first cracking results from the different NSM strengthening configurations and the nature of concrete cracking. Major flexural cracks were observed in all beams after the yielding load was reached. The maximum load capacities of the NSM FRP-strengthened specimens varied from about 65 to 103 kN, depending on the strengthening solution.

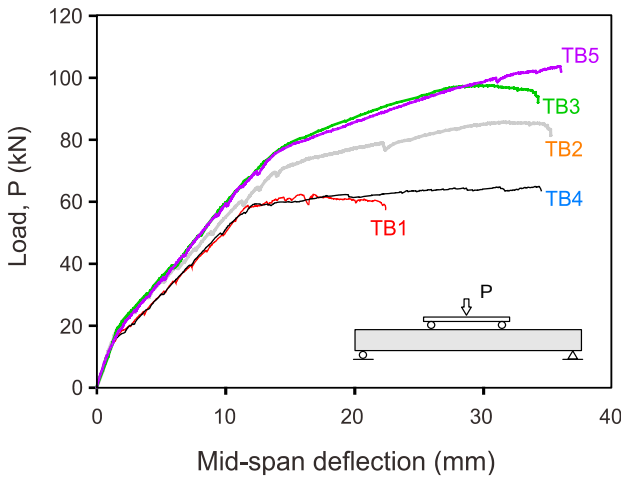

Figure 5. Load-deflection curves of beams TB1 to TB5.

As expected, the failure mode and performance of all tested specimens were controlled by flexure. All the strengthened beams failed due to concrete crushing, except for TB4 whose test was halted when the load started to reduce. Table 4 summarises the main experimental results. In this table, the load-deflection data are classified into three stages: (i) pre-cracked, (ii) pre-yield, and (iii) post-yield. At each stage, the corresponding moment (M), load (P), and deflection (Δ) are reported. At the end of the pre-cracked stage,

the cracking moment (M_{cr}) or cracking load (P_{cr}) of the NSM FRP-strengthened sections were always higher than the corresponding values for TB1. For instance, the ratio $P_{cr}/P_{cr,TB1}$ indicates that the moment was 19% higher for specimen TB3 compared to TB1, which in turn was the highest among the strengthened sections. Beam TB4 (which only had SNSM at the top side) had a similar cracking load to TB1 (difference of 2% only). At the pre-yield stage, all the specimens were already cracked but the longitudinal steel reinforcement remained elastic. The yield moments (M_y) were calculated at the load P_y where gauge S1 showed that the longitudinal steel reinforcement had reached a strain value of 0.002-0.0025. As shown in Table 4, the yield load of the control specimen TB1 was P_y =57.8 kN at a deflection of 11.4 mm. The NSM FRP strengthening solutions increased the yield load by up to 131% (e.g. see TB5).

Table 4. Summary of main experimental results of beams TB1 to TB5.

Stage	Parameters	unit	TB1	TB2	TB3	TB4	TB5
i	M_{cr}	N·mm×10^3	6,442	7,152	7,673	6,573	7,202
	P_{cr}	kN	16.8	18.7	20.0	17.1	18.8
	Δ_{cr}	mm	1.61	1.60	1.81	1.60	1.70
	$P_{cr}/P_{cr,TB1}$	-	1.00	1.11	1.19	1.02	1.12
ii	M_y	N·mm×10^3	22,151	26,730	28,532	22,756	28,969
	P_y	kN	57.8	69.7	74.4	59.3	75.5
	Δ_y	mm	11.4	13.8	13.3	12.1	13.8
	$P_y/P_{y,TB1}$	-	1.00	1.21	1.29	1.03	1.31
	ε_y	-	0.0023	0.0025	0.0024	0.0025	0.0025
iii	M_u	N·mm×10^3	24,237	32,712	37,659	24,965	39,769
	P_u	kN	63.2	85.3	98.2	65.1	103.7
	Δ_u	mm	22.4	34.5	33.7	34.2	35.9
	$P_u/P_{u,TB1}$	-	1.00	1.35	1.55	1.03	1.64

Note: (i) pre-cracked stage, (ii) pre-yield stage, and (iii) post-yield stage.

Significant increases in the yield load were also observed for the strengthened specimens TB2 (+21%) and TB3 (+29%). Moreover, in the post-yield stage, the ultimate

capacities (M_u or P_u) of the NSM FRP-strengthened specimens were 135%, 155%, 103%, and 164% higher for specimens TB2, TB3, TB4 and TB5, respectively. The applications of SNSM at the Bottom of TB3 and TB5 improved their ultimate load capacity, whereas (as expected) the SNSM placed at the top face did not improve noticeably the ultimate load of TB4. Overall, the application of SNSM at the bottom face increased considerably the cracking, yielding and ultimate loads of the strengthened beams. Conversely, the strengthening of beams with NSM CFRP rods inserted in the above the neutral axis is not recommended in practical strengthening applications.

3.2. Cracking behaviour

Cracking in the beam specimens was monitored closely during testing. As the applied load increased, the crack paths were marked at each load step on the front face of the specimen. Observations on the control specimen (TB1) indicated that the first flexural crack always developed close to the beam midspan. More flexural cracks followed within the flexural and shear span regions and existing cracks kept growing in length and width. All strengthened beams generally showed a similar crack development. The first cracking loads ranged from 16-20 kN, and the number of flexural cracks increased and propagated with increasing deflections. Figure 6 shows a complete crack pattern at failure for the unstrengthened and strengthened concrete beams.

Concrete crushing failure was dominant and clearly observed in specimens TB2 (Figure 6(b)) and TB3 (Figure 6(c)). No evidence of debonding failure was observed at the bottom side for BNSM in the case of TB2, nor on the SNSM in the case of TB3. In the case of TB1 and TB4, the test ended after the applied load started to reduce. FRP debonding was observed at the location of SNSM (bottom side) in beam TB5 where the CFRP rods were placed at both top and bottom faces. Whilst the CFRP rods in beams TB4 and TB5 were subjected to compression, no clear evidence of buckling was observed

during or after the tests were halted. Figure 7 shows schematically the complete crack patterns at failure load P_f for the beams. The density of cracks (number/spacing) developed within the flexural zone was measured during the test. Likewise, the crack width (w_f) of a major crack that developed at the midspan was measured at the maximum load level. This information will be compared to analytical models in a subsequent section.

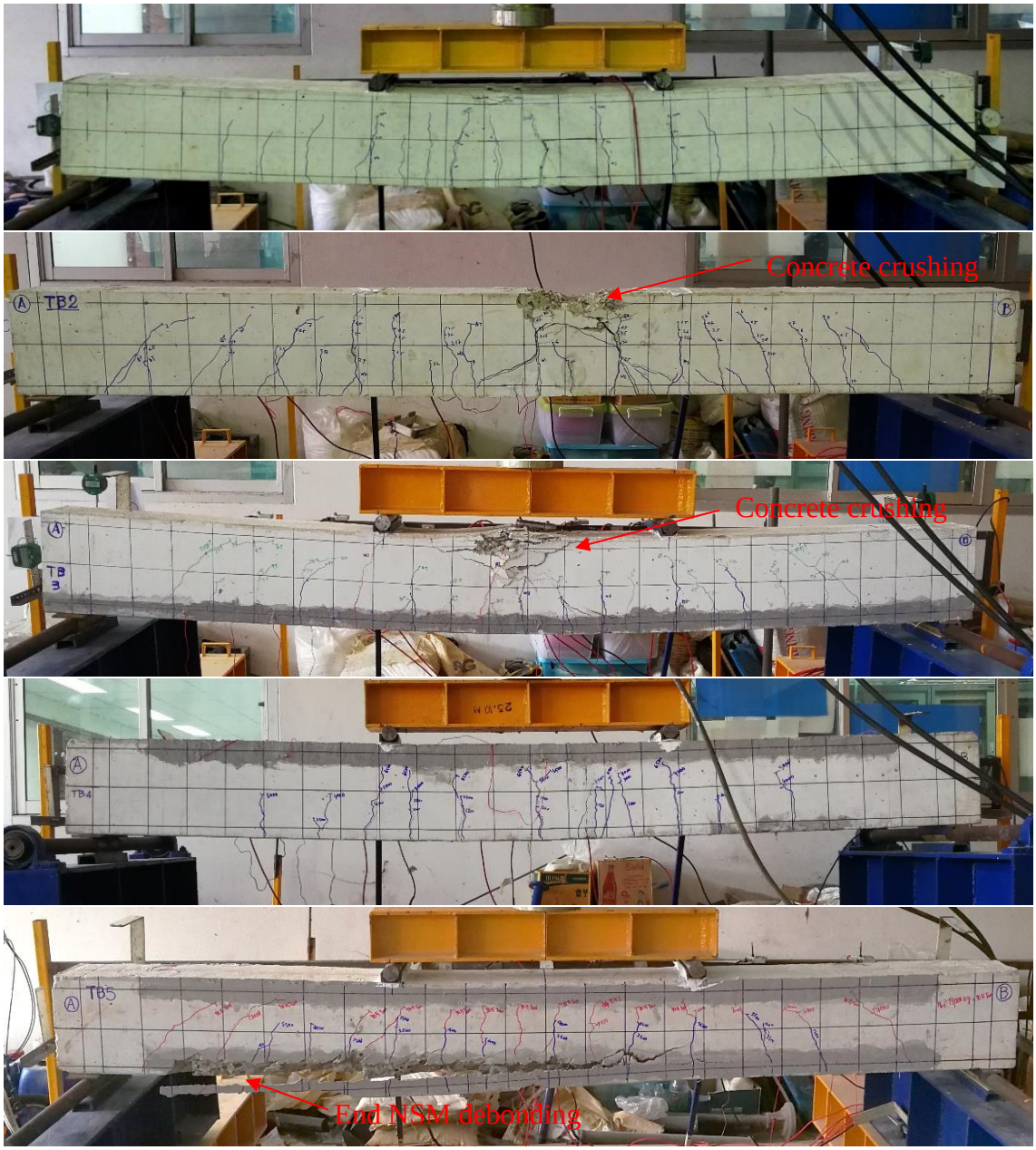

(a) TB1

(b) TB2

(c) TB3

(d) TB4

(e) TB5

Figure 6. Failure modes of tested beams: (a) TB1: tensile crack and steel yielding, (b) TB2: concrete crushing, (c) TB3: concrete crushing, (d) TB4: tensile crack and steel yielding, (e) TB5: end debonding of NSM FRP rod.

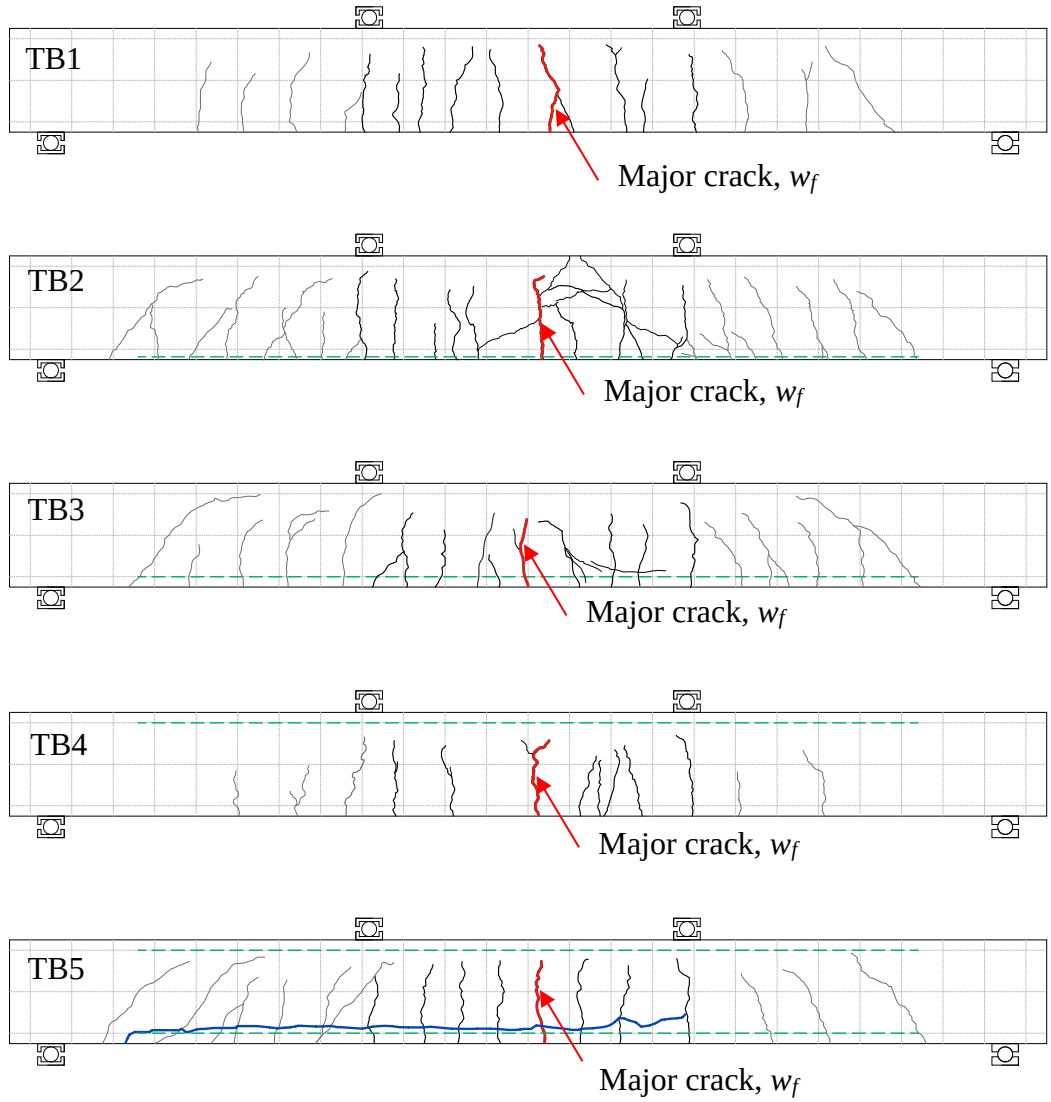

Figure 7. Complete crack maps of tested beams at failure.

3.3. Performance indices of NSM FRP-strengthened beams

Table 5 compares the following results of beams TB2-TB5 over the control beam TB1: ultimate capacity (P_u), ductility at ultimate load (μ_u), ductility at 'failure' load (μ_f), effective pre-yield stiffness (S_e) and energy absorption (ζ). Details on how such results were calculated can be found in Appendix A. The values in Table 5 are expressed as ratios of the test results from the strengthened beams over those from beam TB1 (e.g. S_e / $S_{e,TB1}$

, ζ / ζ_{TB1} etc). The results in Table 5 indicate that the Bottom NSM strengthening solution increased the ultimate load capacity of TB2 by +35%, and that such increase was +55% for the Side NSM strengthened specimen TB3. However, and as expected, the Side NSM at the top of the beam did not significantly increase the ultimate load (+2% only) of TB4. When placing Side NSM at both top and bottom of TB5, the ultimate capacity increased by +64%.

The ductility index derived from the load-deflection curves of the beams represent their capacity to sustain inelastic deformation without decay in load carrying capacity before failure. The results in Table 5 confirm that all strengthened beams had higher μ_u values compared to TB1 due to the provision of the additional flexural reinforcement (NSM CFRP rods). Similar observations were reported by Hosen et al. (2017), who found that beams strengthened with SNSM FRP bars had a good ductility if failure was dominated by flexure, which was attributed to the low elastic modulus of the NSM GFRP bars used in the tests. However, the ductility was found to decrease with increasing amounts of reinforcement. Specimen TB4 had the highest increase in ductility of all the strengthened sections (μ_u = +44%). The provision of NSM CFRP at the compression zone prevented the concrete crushing without reduction of load-carrying capacity and thus allowed a higher deformation before failure. The other two Side NSM beams (TB3 and TB5) had a higher ductility (+29 to +33%) over beam TB1. However, it should be kept in mind that beam TB1 was tested up to the point where its load capacity started to reduce (beam TB1 was strengthened with metal straps in Imjai et al. (2020), and therefore the actual ductility of such beam could have been slightly higher.

The effective pre-yield stiffness (S_e) reflects the ability of the beam to prevent its deformation within the elastic range. The results in Table 5 show that all the strengthened beams had a modest increase in S_e (+2 to +6%) compared to TB1. The NSM FRP rod at

the beam soffit of TB2 led to the highest pre-yield stiffness (+11%). This is because the bottom CFRP rod restrained more effectively the flexural cracking, which initiated at the beam's soffit. To assess the toughness of the beams, the area below the load-deflection curves was calculated to measure the energy absorption (ζ). Table 5 shows that TB5 had the highest energy absorption (+147%). The Bottom NSM TB2 and side NSM TB3 absorbed +114% and +131% more energy than TB1, respectively.

The efficiency (EF) of the NSM CFRP rod is the ratio between the maximum strain value (ε_{max}) recorded in the CFRP rod to the ultimate strain of the FRP rod (ε_{fu}). As shown in Table 5, beam TB4 had the lowest EF (56%). Specimens with bottom and side NSM FRP rods (TB2 and TB3) where concrete crushing dominated at failure, had EF values of 72 % and 84%, respectively. Not surprisingly, TB5 had the highest EF value of 91%.

Table 5. Comparison of strengthening performance indices of beams TB1 to TB5.

Beam	P_u (kN)	μ_u	$\mu_u / \mu_{u,TB1}$	S_e (kN/mm)	$S_e / S_{e,TB1}$	ζ (kN·mm)	ζ / ζ_{TB1}	EF (%)
TB1	63.2	1.96	-	10.50	-	4,497	-	-
TB2	85.3	2.50	1.27	11.69	1.11	9,642	2.14	72
TB3	98.2	2.53	1.29	11.11	1.06	10,402	2.31	84
TB4	65.1	2.83	1.44	10.69	1.02	7,671	1.71	56
TB5	103.7	2.60	1.33	11.06	1.05	11,130	2.47	91

Note: P_u is the ultimate load capacity, μ_u is the ductility at ultimate load, S_e is the effective pre-yield stiffness, ζ is the energy absorption, and EF is the efficiency of NSM CFRP bar.

4. Analysis of beam deflections

This section examines the deflections of the five beams. The analyses were carried out through a moment-curvature approach and a series of 2D finite element (FE) analyses, as explained in the following sections. The results from the FE analyses are also used to compare numerical and experimental crack spacings and crack widths.

4.1. Moment-curvature approach

The midspan deflection of the control and NSM FRP-strengthened beams was predicted using a cracked-sectional analysis based on a moment-curvature approach. To achieve this, the load-deflection response of each beam was divided into three linear phases; (i) pre-cracked ($0 \leq M_a \leq M_{cr}$), (ii) pre-yielded ($M_{cr} \leq M_a \leq M_y$), and (iii) post-yielded ($M_y \leq M_a \leq M_u$), as described in Appendix B. To calculate the midspan deflection, the effective moment of inertia I_e is used to consider the loss of stiffness due to concrete cracking. The current ACI 318 (2019) guidelines adopt the approach proposed by Branson (1966) to calculate I_e. The value I_e provides a transition from the uncracked (I_o) to the fully cracked (I_c) moments of inertia of the section as a function of the ratio between the cracking moment (M_{cr}) and the applied moment (M_a):

$$I_e = \left(\frac{M_{cr}}{M_a}\right)^3 I_o + \left[1 - \left(\frac{M_{cr}}{M_a}\right)^3\right] I_{cr} \tag{1}$$

The midspan deflection, Δ_{mid}, of rectangular beams subjected to four-point bending can be obtained as:

$$\Delta_{mid} = \left(\frac{P}{2}\right) \cdot \left(\frac{L_a}{24 E_c I_e}\right) (3L^2 - 4L_a^2) + \frac{k_s P L}{6 G_c A} \tag{2}$$

where P is the total load, L_a is the clear span of the beam, k_s is the shear correction factor (6/5 for rectangular sections), A is the cross-section area of the beam, and E_c and G_c are Young's and shear modulus of concrete, respectively ($G_c = E_c / 2[1+\upsilon]$, where υ is the Poisson ratio). For RC elements, the effective moment of inertia I_e is often used to calculate the flexural deformation component (first term on the right-hand side of Equation (2)), whereas the shear component (second term of Equation (2)) is considered negligible for slender beams (e.g. see Model Code 2010 (2010)).

4.2. Nonlinear FE analyses

The 2D nonlinear numerical analyses were carried out using the FE software FEMIX (Barros, 2016). Past studies proved that 2-dimensional, plane stress, 8-node quadrilateral elements can be used to predict the load-deflection responses of RC beams with good accuracy (Barros, 2016; Barros et al., 2007; Barros & Fortes, 2005; Yao & Wu, 2016). To simulate the concrete part of all beams, 4-node Serendipity plane stress elements with a 2×2 Gauss-Legendre integration scheme were used. The longitudinal and transverse steel reinforcements were simulated with 2-node linear embedded cable elements with two Gauss-Legendre integration points. For the NSM FRP-strengthened beams TB2 to TB5, a 3-node linear embedded cable element was added to simulate the CFRP rods. A perfect bond was assumed between the concrete and all reinforcements (i.e. bond slip effects were ignored). It should be noted that, in many NSM strengthening applications, the bond-slip of the FRP strips or rods can play in important role in the response, but mainly at high load levels or after yielding of the steel reinforcement. In this article, the main focus is on examining the performance of the beams during the service load stage, and therefore perfect bond between concrete and CFRP bars was assumed in the FE modelling. This is also reasonable because debonding of the FRP rods only occurred in TB5, and only at the end of the test. However, the assumption of the existence of perfect bond between the concrete and NSM FRP strips/rods (and indeed between the concrete and steel bars) should not be extended to other cases to those presented in this article.

The load was applied to the FE model by direct displacement-control at the midspan of the beam. Due to the symmetry of the beams and the load arrangement, only half of each beam was modelled to reduce computational time. The model contains nine layers of elements in the beam height (9 elements @ 16.67 mm), and meshing regions along the half span (72 elements @ 16.67 mm long elements). The element mesh was

also chosen so that the positions of some of the nodes coincided with the location of the LVDTs and applied loads in the test setup. Examples of a half symmetry FE model for beams TB1, TB2 and TB3 are shown in Figure 8.

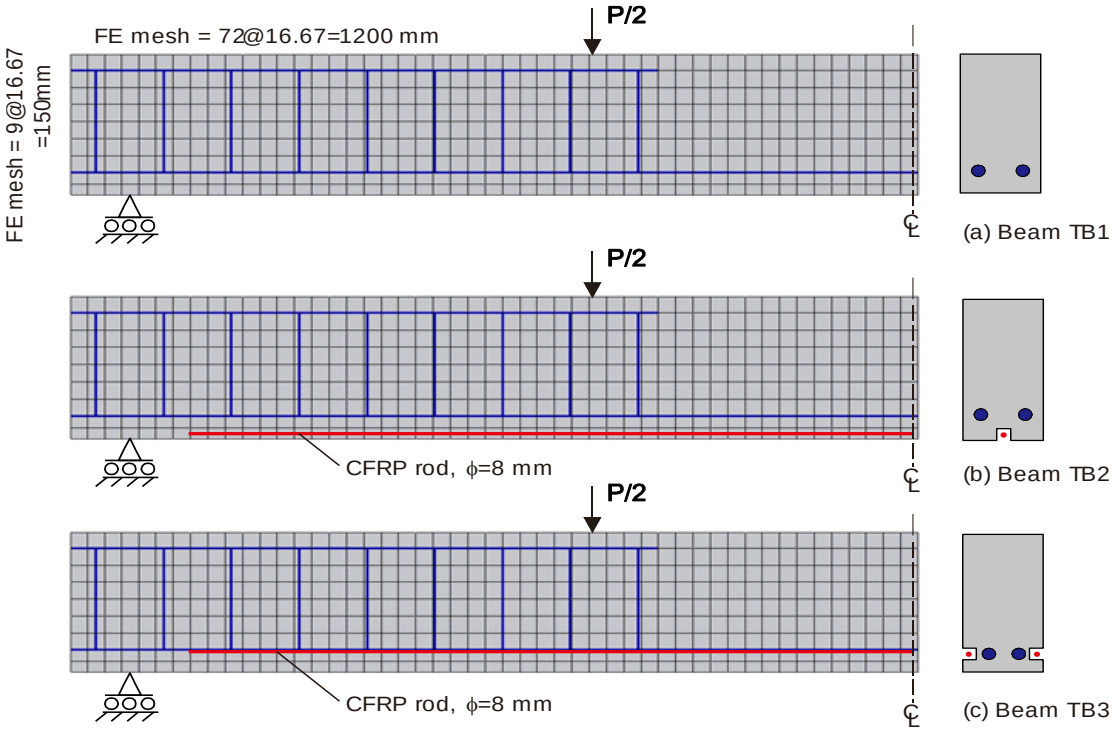

Figure 8. Typical finite element mesh of beams a) TB1, b) TB2 and c) TB3.

All concrete parameters were calculated using the compressive strength of the concrete, f_c, and the recommendations in *fib* Model Code 2010 (2010). The behaviour of the concrete was modelled using a multi-fixed smeared crack model available in FEMIX (Ventura-Gouveia et al., 2011). The fracture Mode I in this model is simulated by a trilinear tensile softening diagram, as shown in Figure 9(a). The parameters ξ and α represent the ratio between the strain and stress at each point of the trilinear tensile-softening diagram (fracture Mode I), respectively. The values used in all analyses were $\xi_1 = 0.15$ & $\alpha_1 = 0.75$, and $\xi_2 = 0.4$ & $\alpha_2 = 0.4$. The Mode I fracture energy used was $G_f =$ 0.12 N/mm. The crack bandwidth (Figure 9(a)) was estimated using the square root of the area of the integration point. The behaviour of the longitudinal and transverse steel

bars was modelled using the stress-strain represented in Figure 9(b). A linear stress-strain relationship was adopted for modelling the NSM-CFRP rods. The values of the stress-strain curves defining the behaviour of the steel bars and CFRP rods were defined using the properties of each material, as determined by the laboratory test results.

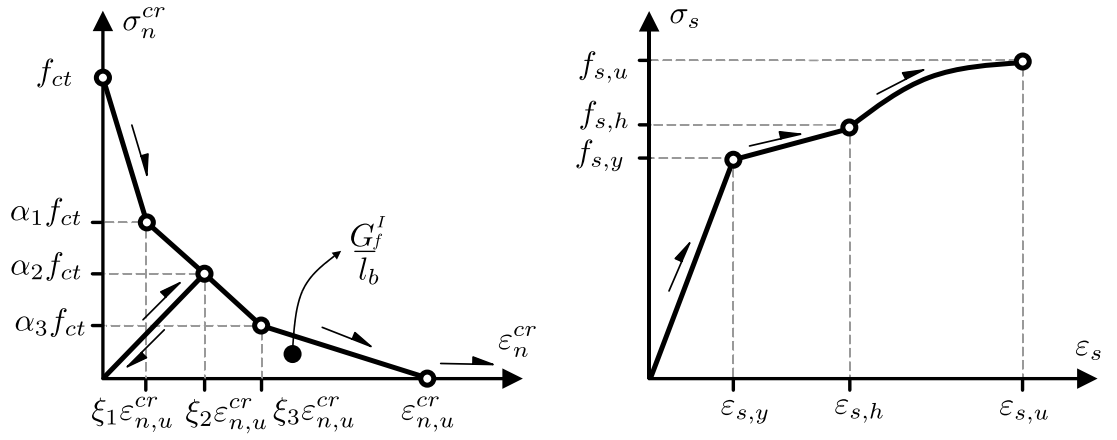

(a) Tension softening diagram (b) Uniaxial constitutive model of the steel bars

Figure 9. Constitutive models of materials for FE analyses (a) tension softening model for concrete, (b) constitutive model for steel bars.

The constitutive material models adopted in the simulations led to a system of nonlinear equations that was solved using the Newton-Raphson method. The developed model includes implicit Euler backward algorithms and consistent tangent operators (Barros et al., 2007; Barros & Fortes, 2005). The following section compares the results from the analyses in this section with the measured load-deflection to evaluate the reliability of existing calculation methods.

4.3. Comparison of calculated and experimental deflections

Figure 10 compares the experimental (*Exp.*) midspan load-deflections with the results from a moment-curvature approach (*Anl.*) and FE analyses (*FE*) for all beams. It should be noted that the concrete tensile strength used to determine the cracking moment and

cracking load was derived from an inverse analysis to account indirectly for the variability of concrete, size effects, as well as shrinkage effects on the initial strain state within the element (Bischoff, 2005).

Overall, the results in Figure 10 indicate that the moment-curvature approach predicts reasonably well the deflections at the first flexural cracking load and yield load. For the NSM FRP-strengthened beams, the load-deflection curves from the moment-curvature approach are slightly stiffer than the experimental ones. Note that the stiffness of TB2 and TB3 decreased shortly after yielding as the beams were reaching failure, which was dominated by concrete crushing at the top of the beams. This is attributed to the fact that a perfect bond was assumed at the reinforcement/concrete interface.

After yielding, the analytical predictions tend to underestimate the deflections, especially when major cracks occur (e.g. TB2 and TB4). Note also that the adhesive resin used to fill the groove of the CFRP rod was not accounted for in the models. Therefore, the predictions were expected to be stiffer than the experimental values. Based on these results, it is evident that the moment-curvature approach tends to underestimate deflections after major cracks occur. This can be attributed to an overall underestimation of deformation due to several cracks opening simultaneously (such as shear cracks), an effect that is more pronounced after the onset of diagonal cracking as reported previously (Imjai et al. 2016). To accurately predict the beam deflections at higher load levels, shear crack-induced deflections should be taken into an account.

Figure 10 also shows that, in general, the FE models can simulate well the aspects that control deflections such as crack initiation, stiffness degradation, yield initiation of the steel bars, and ultimate capacity. The results agree well with the predicted cracking load and the corresponding deflection before major flexural cracks appear (i.e. crack w_f

in Figure 7). After large flexural cracks form, the deflection from the FE model was always lower than the measured deflection. However, the errors between the FE results and experimental deflections were less than 5%, except for TB2 and TB3 where convergence issues with the Newton-Raphson iterative procedure led to larger errors by up to 15% at ultimate load.

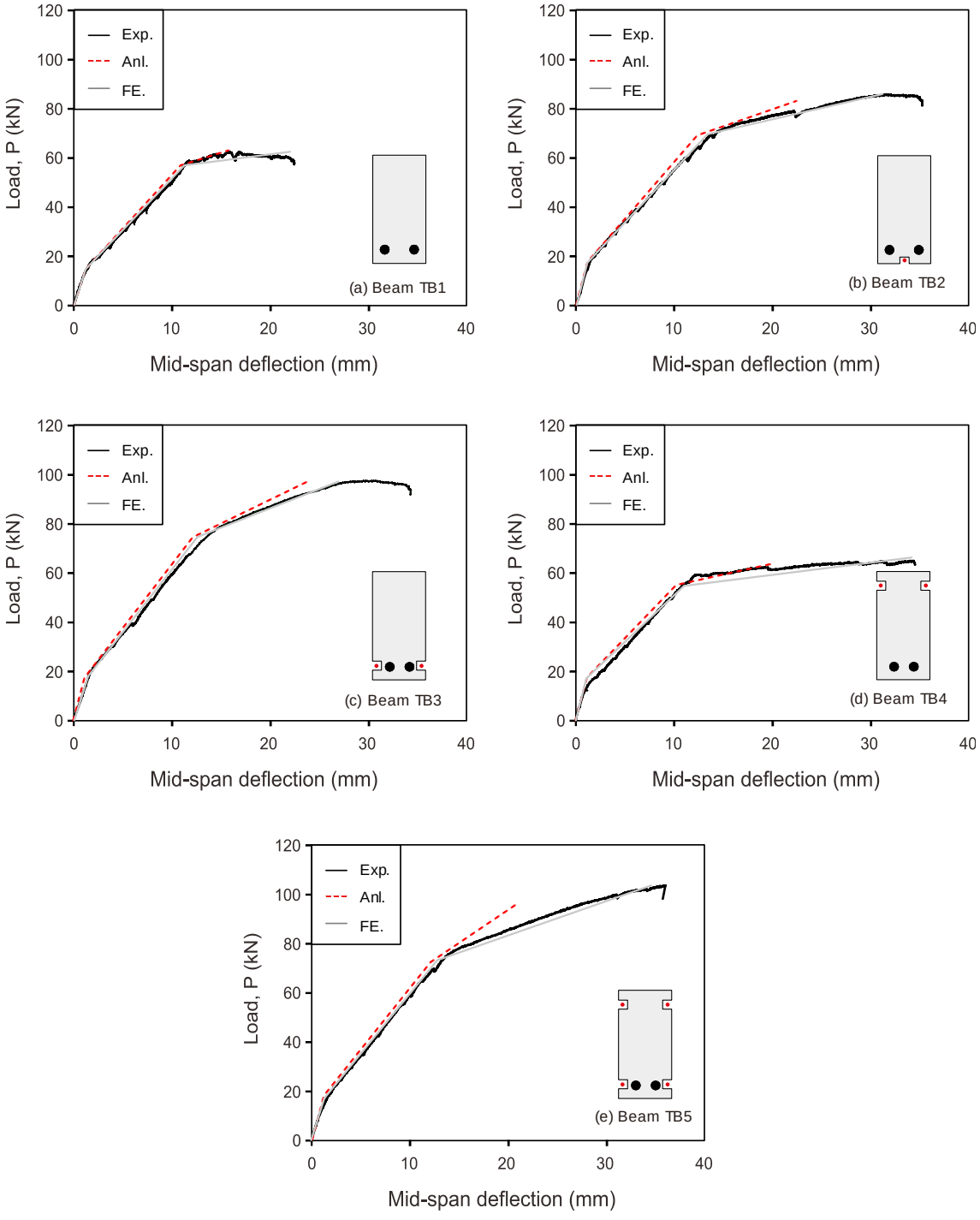

Figure 10. Experimental vs predicted load-deflection curves of beams TB1 to TB5.

Figure C1 in Appendix C shows an example of a typical crack pattern (beam TB1) obtained from the FE analyses. The results show that, in general and for all the beams, the distribution of the flexural cracks at the midspan of the beams agreed reasonably well with the experimental results. Likewise, Figure C2 in Appendix C shows a typical evolution of stresses in the steel bars and CFRP rod during the FE simulation. The results in the figure are for beam TB2, which is representative of the other strengthened beams. As expected, the stress in the CFRP rod increases linearly with an increase in the load, whereas the stresses in the steel bars are practically constant after yielding.

4.4. Comparison of flexural crack spacing and crack width

Eurocode 2 (EC2) (2004) calculates the flexural crack spacing as a function of the modular ratio and the location of the neutral axis in the composite section. Accordingly, Equation (3) can be used to calculate the maximum crack spacing (S_{max}) in the constant moment zone of the beams:

$$S_{max} = 3.4c + 0.425k_1k_2\frac{\varphi_f}{\rho_{ef}} \tag{3}$$

where ρ_{ef} is the effective reinforcement ratio, that can be obtained as follows:

$$\rho_{ef} = \frac{A_s + n_{SNSM}A_{SNSM}}{A_{cef}} \tag{4}$$

and where A_{cef} is the area of the concrete in tension, that can be obtained as follows:

$$A_{cef} = \min\begin{Bmatrix} 2.5bc \\ b\,(h-y)/3 \end{Bmatrix} \tag{5}$$

where c is the concrete cover, k_1 is the bond coefficient (0.80 and 1.6 for high bond bars and plain bars, respectively), k_2 is the strain distribution coefficient (0.50 and 1.0 for bending and pure tension, respectively), φ_f is the diameter of the FRP rod, A_s is the area of the longitudinal reinforcement (in tension), A_{SNSM} is the area of the NSM FRP rod, n_{SNSM} is the number of NSM FRP rods, h is the depth of the beam, b is the width of the beam, and y is the neutral axis depth.

Figure 11 compares the (average) measured crack spacing at the constant moment zone and the corresponding maximum crack spacing calculated using the EC2 approach. The results show that the measured crack spacings were 90, 85, 82, 102, and 110 mm for TB1, TB2, TB3, TB4, and TB5, respectively. Comparatively, the maximum crack spacings calculated by EC2 were 120, 117, 116, 119, and 116 mm for TB1, TB2, TB3, TB4, and TB5, respectively. Overall, the EC2 model gives larger crack spacings (+17% on average) compared to the values recorded in the tests. The closer crack spacing in the strengthened beams can be attributed to the development of a more distributed bond along the NSM FRP rods. Similar observations were also reported in other studies (Hosen et al., 2017, 2018, 2015) that examined the behaviour of RC beams strengthened with side NSM FRP bars.

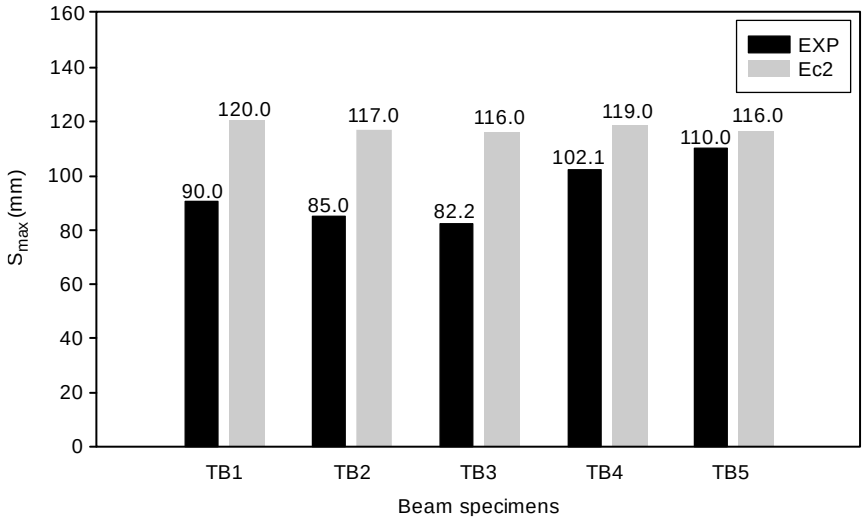

Figure 11. Experimental vs Eurocode 2 calculation of crack spacing of beams TB1 to TB5

The flexural crack width of the beams was also measured during the tests. The last reading was taken at the maximum load level as measurements had to be halted after that due to safety reasons. The crack width w_f of the beams can be calculated using Equation (6), which is given in EC2. The equation depends on the maximum crack spacing (S_{max}) and on the strain in the longitudinal reinforcement (ε_{sm}), where the latter accounts for the tension softening and the mean strain in the concrete between cracks (ε_{cm}):

$$w_f = S_{max}(\varepsilon_{sm} - \varepsilon_{cm}) \tag{6}$$

The strain ε_{sm} can be computed using Equation (7):

$$(\varepsilon_{sm} - \varepsilon_{cm}) = \frac{\sigma_s}{E_s} - \frac{k_t f_t'\left(1 + n\rho_{eff}\right)}{E_s \rho_{eff}} \geq 0.6\frac{\sigma_s}{E_s} \tag{7}$$

where k_t is the factor of the duration of loading (0.4 and 0.6 for long-term and short-term loading, respectively), f_t' is the tensile strength of the concrete, n is the modular ratio between steel and concrete, ρ_{eff} is the effective reinforcement ratio, and the rest of the terms are as defined before.

Figure 12 compares the measured crack width and the results given by EC2 at different loading stages. At the end of the pre-cracked stage, the measured crack width of TB1 was about 0.09 mm, which is very close to the calculated value of 0.10 mm. Also, all strengthened beams had narrower crack widths compared to TB1 (Figure 12(a)). In the pre-yield stage, the calculated crack widths agree very well with the measured values, with small differences of 10% (e.g. TB2). At yielding, the observed crack widths were < 0.5 mm and therefore compliant with the serviceability limits suggested by ACI 440.1R.

In the post-yield stage, TB1 had the widest cracks (0.31 mm), whereas TB2, TB3, TB4 and TB5 had narrower crack widths (0.29, 0.28, 0.27 and 0.24 mm respectively). The crack widths calculated by EC2 were only 5% higher than the measurements. Based on these observations, it is clear that the use of FRP rods helped to control the crack widths in the NSM FRP-strengthened low-strength RC beams. Whilst the crack widths calculated by EC2 agree well with the test results presented in this article, further tests on different concrete strengths and numerical research are necessary to fully validate this observation. This is particularly true because the actual characteristics of the cracks rely heavily (among others) on concrete properties such as the compressive strength, as well as the (highly variable) tensile strength.

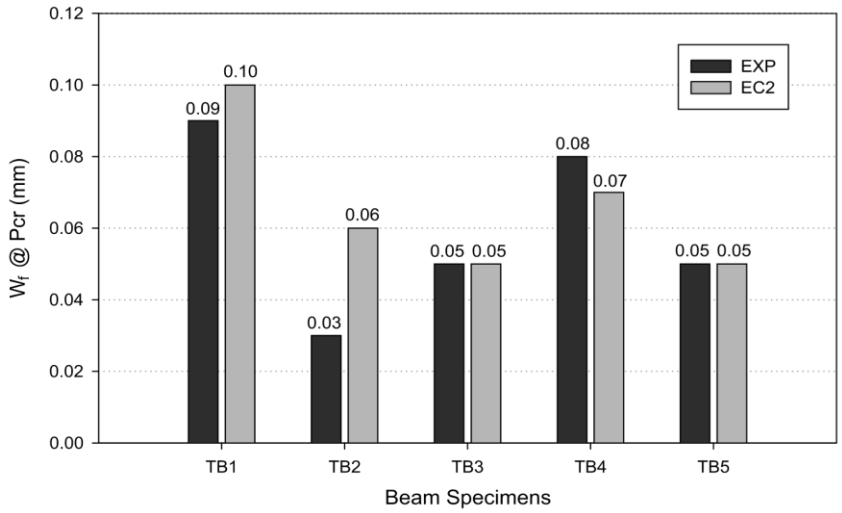

(a) Crack widths at the end of pre-cracked stage

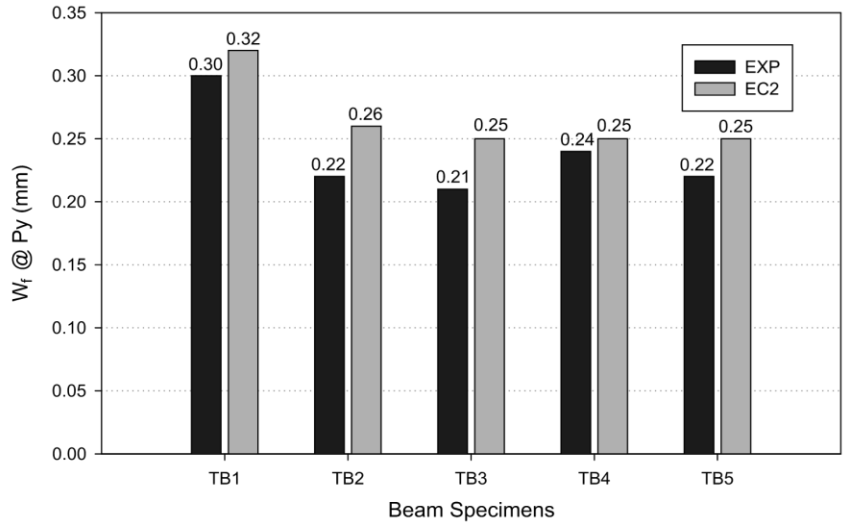

(b) Crack widths in the pre-yield load level

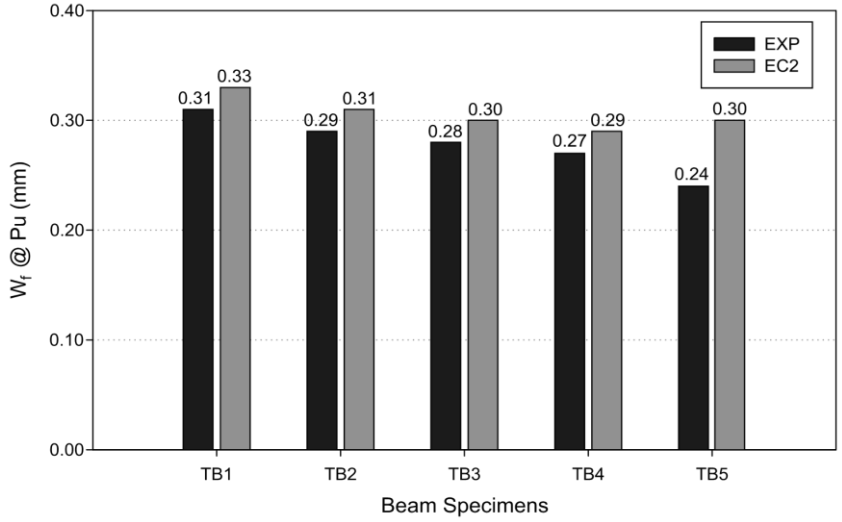

(c) Crack width at ultimate load level

Figure 12. Experimental vs Eurocode 2 calculations of crack widths of beams TB1 to TB5 at different loading stages.

5. Conclusions

This article presented an experimental and numerical study aimed to investigate the behaviour of RC beams strengthened with Side NSM (SNSM) or Bottom NSM (BNSM) CFRP rods. Based on the results of this study, the following conclusions can be drawn:

- The SNSM strengthening solutions increased the cracking load of the beams (by up to 19%). Moreover, the yield and ultimate load-carrying capacities of the NSM FRP-strengthened beams increased notably by up to 31% and 64%, respectively (beam TB5).
- The results from nonlinear Finite Element (FE) analyses matched well the experimental results up to failure of the beams, which confirms the effectiveness of the modelling approach used in the FE software.
- The moment-curvature and FE analyses predict well the deflections within 20% and 10% of accuracy at failure, respectively.
- Larger experimental deflections were observed after major cracks occurred. To accurately predict the beam deflection at a higher load level, the shear crack-induced deflection should be taken into an account.
- The models to calculate the maximum crack spacing and crack width currently included in Eurocode 2 match well the experimental values of the beams presented in this study. However, further research is necessary to confirm if these observations are valid for other case studies.

6. Acknowledgements

This research was funded by National Research Council of Thailand (NRCT5-RSA63019-04). This research was financially supported by the new strategic research project (P2P) fiscal year 2022, Walailak University, Thailand. The project was also supported by Thailand Science

Research and Innovation Fund (FRB650082/0227) and the Capacity Enhancement and Driving Strategies for Bilateral and Multilateral Cooperation for 2021 (Thailand and United Kingdom).

7. References:

Abid, S. R., & Al-lami, K. (2018). Critical review of strength and durability of concrete beams externally bonded with FRP. *Cogent Engineering*, 5(1), 1–27. http://dx.doi.org/10.1080/23311916.2018.1525015

ACI Committee 318. (2019). Building Code Requirements for Structural Concrete : (ACI 318-19) ; and Commentary (ACI 318R-19). MI; American Concrete Institute: Farmington Hills.

ACI Committee 440. (2017). ACI 440.2R-17: Guide for the design and construction of externally bonded FRP systems for strengthening existing structures. American Concrete Institute.

Al-Mahmoud, F., Castel, A., François, R., & Tourneur, C. (2009). Strengthening of RC members with near-surface mounted CFRP rods. Composite Structures, 91(2), 138–147.

Al-Saadi, N. T. K., Mohammed, A., Al-Mahaidi, R., & Sanjayan, J. (2019). Performance of NSM FRP embedded in concrete under monotonic and fatigue loads: state-of-the-art review. *Australian Journal of Structural Engineering*, 20(2), 89–114. http://dx.doi.org/10.1080/13287982.2019.1605686

Barros, J. A. O. (2016). Debilities and strengths of FEM-based constitutive models for the material nonlinear analysis of steel fiber reinforced concrete structures. V. Saouma, J. Bolander, & E. Landis (Eds.), In: *9th International Conference on Fracture Mechanics of Concrete and Concrete Structures*, FraMCoS-9. California.

Barros, J. A. O., Dias, S. J. E., & Lima, J. L. T. (2007). Efficacy of CFRP-based techniques for the flexural and shear strengthening of concrete beams. *Cement and Concrete Composites*, 29(3), 203–217. http://dx.doi.org/10.1016/j.cemconcomp.2006.09.001

Barros, J. A. O., & Fortes, A. S. (2005). Flexural strengthening of concrete beams with CFRP laminates bonded into slits. *Cement and Concrete Composites*, 27(4), 471–480. http://dx.doi.org/10.1016/j.cemconcomp.2004.07.004

Bilotta, A., Faella, C., Martinelli, E., & Nigro, E. (2013). Design by testing procedure for intermediate debonding in EBR FRP strengthened RC beams. *Engineering Structures*, 46, 147–154. http://dx.doi.org/10.1016/j.engstruct.2012.06.031

Bilotta, Antonio, Ceroni, F., Nigro, E., & Pecce, M. (2015). Efficiency of CFRP NSM strips and EBR plates for flexural strengthening of RC beams and loading pattern influence. *Composite Structures*, 124, 163–175. http://dx.doi.org/10.1016/j.compstruct.2014.12.046

Bischoff, P. H. (2005). Re-evaluation of deflection prediction for concrete beams reinforced with steel and fiber reinforced polymer bars. *Journal of Structural Engineering*, 131(5), 752–767.

Branson, D. E. (1966). Deflections of reinforced concrete flexural members. *Journal of the American Concrete Institute*, 63(6), 637-667.

British Standard Institution. (1983a). BS 1881-116:1983 Testing Concrete - Part 116: Method for Determination of Compressive Strength of Concrete Cubes. BSI, London, UK.

British Standard Institution. (1983b). BS 1881-117:1983 Testing Concrete - Part 117: Method for Determination of Tensile Splitting Strength. BSI, London, UK.

British Standard Institution. (1983c). BS 1881-118:1983 Testing Concrete - Part 118: Method for Determination of Flexural Strength. BSI, London, UK.

CEB-FIB 2010. (2010). Model Code Design Code. Thomas Telford Services Ltd, London.

De Lorenzis, L., & Teng, J. G. (2007). Near-surface mounted FRP reinforcement: An emerging technique for strengthening structures. *Composites Part B: Engineering*, 38(2), 119–143. http://dx.doi.org/10.1016/j.compositesb.2006.08.003

Eurocode 2 (2004): Design of Concrete Structures: Part 1–1: General Rules and Rules for Buildings.

fib Task Group 5.1. (2019). Fib Bulletin 90 Externally applied FRP reinforcement for concrete structure. International Federation for Structural Concrete.

German Committee for Reinforced Concrete. (2013). DAfStb Heft 595 Erläuterungen und Beispiele zur DAfStb-Richtlinie Verstärken von Betonbauteilen mit geklebter Bewehrung. Berlin, Germany.

Gopinath, S., Murthy, A. R., & Patrawala, H. (2016). Near surface mounted strengthening of RC beams using basalt fiber reinforced polymer bars. *Construction and Building Materials*, 111, 1–8. http://dx.doi.org/10.1016/j.conbuildmat.2016.02.046

Gravina, R., Aydin, H., & Visintin, P. (2018). Review of near-surface mounted FRP plates in the strengthening of continuous flexural members and bond behaviour. *Australian Journal of Civil Engineering*, 16(2), 158–165. http://dx.doi.org/10.1080/14488353.2018.1537594

Gudonis, E., Timinskas, E., Gribniak, V., Kaklauskas, G., Arnautov, A. K., & Tamulėnas, V. (2014). FRP Reinforcement for Concrete Structures: State-of-the-Art Review of Application and Design. *Engineering Structures and Technologies*, 5(4), 147–158. http://dx.doi.org/10.3846/2029882x.2014.889274

Hernandez, D. A., & Orlandi, M. O. (2016). Mechanical properties of composites materials sikacarbodur 512, sikadur 30 and sikadur 330. Paper presented at the 22o CBECiMat - Congresso Brasileiro de Engenharia e Ciência dos Materiais. Natal, RN, Brasil.

Hosen, M. A., Alengaram, U. J., Jumaat, M. Z., Sulong, N. H. R., & Darain, K. M. ud. (2017). Glass Fiber Reinforced Polymer (GFRP) Bars for Enhancing the Flexural Performance of RC Beams Using Side-NSM Technique. *Polymers*, 9(12), 180. http://dx.doi.org/10.3390/polym9050180

Hosen, M. A., Jumaat, M. Z., Alengaram, U. J., & Ramli Sulong, N. H. (2018). CFRP strips for enhancing flexural performance of RC beams by SNSM strengthening technique. *Construction and Building Materials*, 165, 28–44. http://dx.doi.org/10.1016/j.conbuildmat.2017.12.052

Hosen, M. A., Jumaat, M. Z., & Islam, A. B. M. S. (2015). Side Near Surface Mounted (SNSM) technique for flexural enhancement of RC beams. *Materials and Design*, 83, 587–597. http://dx.doi.org/10.1016/j.matdes.2015.06.035

Imjai, T., & Garcia, R. (2017). Performance of damaged RC beams repaired and/or strengthened with FRP sheets: An experimental investigation. Paper presented at the Mechanics of Structures and Materials: Advancements and Challenges - Proceedings of the 24th Australasian Conference on the Mechanics of Structures and Materials, ACMSM24 2016.

Imjai, T., Guadagnini, M., Garcia, R., & Pilakoutas, K. (2016). A practical method for determining shear crack induced deformation in FRP RC beams. *Engineering Structures*, 126, 353-364. http://dx.doi.org/10.1016/j.engstruct.2016.08.007

Imjai, T, Phumkesorn, J., Pansuk, W., & Garcia, R. (2017). EBR FRP-strengthened beams: A FEA study on end-plate effects. Paper presented at the Proceedings of the 6th Asia-Pacific Conference on FRP in Structures, APFIS 2017.

Imjai, Thanongsak, Setkit, M., Garcia, R., & Figueiredo, F. P. (2020). Strengthening of damaged low strength concrete beams using PTMS or NSM techniques. *Case Studies in Construction Materials*, 13, e00403. http://dx.doi.org/https://doi.org/10.1016/j.cscm.2020.e00403

Kim, K.-H. E., & Andrawes, B. (2017). Retrofitting of bridge abutment timber piles using fiber-reinforced polymer composites. *Journal of Structural Integrity and Maintenance*, 2(1), 29–38. http://dx.doi.org/10.1080/24705314.2017.1280591

Kim, Y. J. (2019). State of the practice of FRP composites in highway bridges. *Engineering Structures*, 179, 1–8. http://dx.doi.org/10.1016/j.engstruct.2018.10.067

Laraba, A., Chikh, N., Mesbah, H., Djebbar, N., & Belouar, A. (2014). Experimental evaluation of damaged rectangular reinforced concrete beams repaired with near surface mounted carbon fibre reinforced polymer. *Materials Research Innovations*, 18, S6-10-S6-13. http://dx.doi.org/10.1179/1432891714Z.000000000923

Nanni, A. (2003). North American design guidelines for concrete reinforcement and strengthening using FRP: Principles, applications and unresolved issues. *Construction and Building Materials*, 17(6–7), 439–446. http://dx.doi.org/10.1016/S0950-0618(03)00042-4

Oehlers, Deric J. (2001). Development of design rules for retrofitting by adhesive bonding or bolting either FRP or steel plates to RC beams or slabs in bridges and buildings. *Composites - Part A: Applied Science and Manufacturing*, 32(9), 1345–1355.

Oehlers, Deric John. (1992). Reinforced Concrete Beams with Plates Glued to their Soffits. *Journal of Structural Engineering*, 118(8), 2023–2038. http://dx.doi.org/10.1061/(ASCE)0733-9445(1992)118:8(2023)

Oller, E., Cobo, D., & Mari, A. R. (2011). Laminate debonding process of FRP-strengthened beams. *Structure and Infrastructure Engineering*, 7(1-2), 131-146.

Osman, B. H., Wu, E., Ji, B., & Abdulhameed, S. S. (2017). Repair of Pre-cracked Reinforced Concrete (RC) Beams with Openings Strengthened Using FRP Sheets Under Sustained Load. *International Journal of Concrete Structures and Materials*, 11(1), 171–183. http://dx.doi.org/10.1007/s40069-016-0182-3

Pachalla, S. K. S., & Prakash, S. S. (2017). Efficient near surface mounting CFRP strengthening of pretensioned hollow core slabs with opening – An experimental study. *Composite Structures*, 162, 28–38. http://dx.doi.org/10.1016/j.compstruct.2016.11.072

Parretti, R., & Nanni, A. (2004). Strengthening of RC members using near-surface mounted FRP composites: Design overview. *Advances in Structural Engineering*, 7(6), 469–483. http://dx.doi.org/10.1260/1369433042863198

Parvin, A., & Shah, T. S. (2016). Fiber reinforced polymer strengthening of structures by near-surface mounting method. *Polymers*, 8(8). 298 http://dx.doi.org/10.3390/polym8080298

Pešić, N., & Pilakoutas, K. (2003). Concrete beams with externally bonded flexural FRP-reinforcement: Analytical investigation of debonding failure. *Composites Part B: Engineering*, 34(4), 327–338.

Rabinovitch, O., & Frostig, Y. (2003). Experiments and analytical comparison of RC beams strengthened with CFRP composites. *Composites Part B: engineering*, 34(8), 663-677.

Rezazadeh, M., Ramezansefat, H., & Barros, J. (2016). NSM CFRP Prestressing Techniques with Strengthening Potential for Simultaneously Enhancing Load Capacity and Ductility Performance. *Journal of Composites for Construction*, 20(5), 04016029. http://dx.doi.org/10.1061/(asce)cc.1943-5614.0000679

Sabau, C., Popescu, C., Sas, G., Schmidt, J. W., Blanksvärd, T., & Täljsten, B. (2018). Strengthening of RC beams using bottom and side NSM reinforcement. *Composites Part B: Engineering*, 149, 82–91. http://dx.doi.org/10.1016/j.compositesb.2018.05.011

Sena-Cruz, J., Barros, J., Bianco, V., Bilotta, A., Bournas, D., Ceroni, F., Triantafillou, T. (2016). NSM systems. *RILEM State-of-the-Art Reports*, 19, 303–348. http://dx.doi.org/10.1007/978-94-017-7336-2_8

Setunge, S., & Nezamian, A. (2004). A case study of application of FRP composites in strengthening of the reinforced concrete headstock of a bridge structure. FRP

Composites in Civil Engineering - CICE 2004, 11(5), 939–945. http://dx.doi.org/10.1201/9780203970850.ch107

Sharaky, I. A., Reda, R. M., Ghanem, M., Seleem, M. H., & Sallam, H. E. M. (2017). Experimental and numerical study of RC beams strengthened with bottom and side NSM GFRP bars having different end conditions. *Construction and Building Materials*, 149, 882–903. http://dx.doi.org/10.1016/j.conbuildmat.2017.05.192

Sharaky, I. A., Torres, L., Comas, J., & Barris, C. (2014). Flexural response of reinforced concrete (RC) beams strengthened with near surface mounted (NSM) fibre reinforced polymer (FRP) bars. *Composite Structures*, 109, 8–22. http://dx.doi.org/10.1016/j.compstruct.2013.10.051

Shukri, A. A., Hosen, M. A., Muhamad, R., & Jumaat, M. Z. (2016). Behaviour of precracked RC beams strengthened using the side-NSM technique. *Construction and Building Materials*, 123, 617–626. http://dx.doi.org/10.1016/j.conbuildmat.2016.07.066

Siddika, A., Mamun, M. A. Al, Alyousef, R., & Amran, Y. H. M. (2019). Strengthening of reinforced concrete beams by using fiber-reinforced polymer composites: A review. *Journal of Building Engineering*, 25, 100798. http://dx.doi.org/10.1016/j.jobe.2019.100798

Siddika, A., Mamun, M. A. Al, Ferdous, W., & Alyousef, R. (2020). Performances, challenges and opportunities in strengthening reinforced concrete structures by using FRPs – A state-of-the-art review. *Engineering Failure Analysis*, 111, 104480. http://dx.doi.org/10.1016/j.engfailanal.2020.104480

Smith, S. T., & Teng, J. G. (2002a). FRP-strengthened RC beams. I: review of debonding strength models. *Engineering Structures*, 24(4), 385–395. http://dx.doi.org/10.1016/S0141-0296(01)00105-5

Smith, S. T., & Teng, J. G. (2002b). FRP-strengthened RC beams. II: Assessment of debonding strength models. *Engineering Structures*, 24(4), 397–417.

Spadea, G., Bencardino, F., Sorrenti, F., & Swamy, R. N. (2015). Structural effectiveness of FRP materials in strengthening RC beams. *Engineering Structures*, 99, 631–641.

Szabó, Z. K., & Balázs, G. L. (2007). Near surface mounted FRP reinforcement for strengthening of concrete structures. *Periodica Polytechnica Civil Engineering*, 51(1), 33–38. http://dx.doi.org/10.3311/pp.ci.2007-1.05

Teng, J. G., Yu, T., & Fernando, D. (2012). Strengthening of steel structures with fibre-reinforced polymer composites. *Journal of Constructional Steel Research*, 78, 131–143. http://dx.doi.org/10.1016/j.jcsr.2012.06.011

Teng, J. G., Yuan, H., & Chen, J. F. (2006). FRP-to-concrete interfaces between two adjacent cracks: Theoretical model for debonding failure. *International Journal of Solids and Structures*, 43(18–19), 5750–5778. http://dx.doi.org/10.1016/J.IJSOLSTR.2005.07.023

Ventura-Gouveia, A., Barros, J. A. O., & Azevedo, A. F. M. (2011). Crack constitutive model for the prediction of punching failure modes of fiber reinforced concrete laminar structures. *Computers and Concrete*, 8, 735–755.

Yao, J., Teng, J. G., & Lam, L. (2005). Experimental study on intermediate crack debonding in FRP-strengthened RC flexural members. *Advances in Structural Engineering*, 8(4), 365–395. http://dx.doi.org/10.1260/136943305774353106

Yao, L.-Z., & Wu, G. (2016). Nonlinear 2D Finite-Element Modeling of RC Beams Strengthened with Prestressed NSM CFRP Reinforcement. *Journal of Composites for Construction*, 20(4), 04016008. http://dx.doi.org/10.1061/(asce)cc.1943-5614.0000659

Zhang, H., & Smith, S. T. (2017). Influence of plate length and anchor position on FRP-to-concrete joints anchored with FRP anchors. *Composite Structures*, 159, 615–624.

Zhang, S. S., Yu, T., & Chen, G. M. (2017). Reinforced concrete beams strengthened in flexure with near-surface mounted (NSM) CFRP strips: Current status and research needs. *Composites Part B: Engineering*, 131, 30–42. http://dx.doi.org/10.1016/j.compositesb.2017.07.072

Zhou, A., Qin, R., Feo, L., Penna, R., & Lau, D. (2017). Investigation on interfacial defect criticality of FRP-bonded concrete beams. *Composites Part B: Engineering*, 113, 80–90.

Appendix A: Strengthening performance indices

Ductility

The ductility of the tested beam at ultimate (μ_u) is the ratio of deflection at ultimate (Δ_u) and deflection at yield load (Δ_y).

$$\mu_u = \frac{\Delta_u}{\Delta_y} \quad \text{(A.1)}$$

Effective pre-yield stiffness

The effective pre-yield stiffness (S_e) of the tested beam can be determined from the slope of the load-deflection in the linear response of the experimental load-deflection response.

$$S_e = slope\ (Py, \Delta_y) \quad \text{(A.2)}$$

Efficiency of NSM FRP bar

The efficiency of the NSM FRP bar is the ratio between the maximum strain value (ε_{max}) induced the NSM FRP bar to the ultimate strain of the FRP bar (ε_{fu}).

$$EF = \frac{\varepsilon_{max}}{\varepsilon_{fu}} \quad \text{(A.3)}$$

Energy absorption

The energy absorption (ζ) is expressed as the total energy dissipated during the deformation of the tested specimen and can be determined from the area of the experimental load-deflection response after yield load.

$$\zeta = \int_{\Delta_y}^{\Delta_f} P(x).dx \quad \text{(A.4)}$$

Appendix B: Moment-curvature approach for RC beam with NSM strengthening

The capacity of NSM FRP-strengthened beams can be calculated using cracked sectional analysis. Force equilibrium and strain compatibility requirements are used to calculate the ultimate load of the original and strengthened beams.

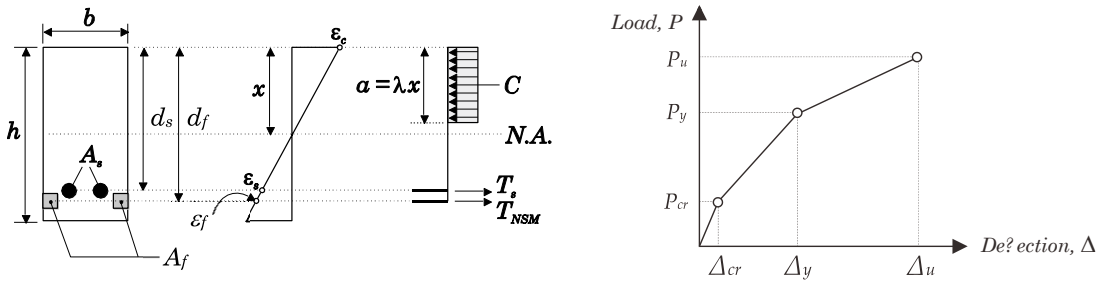

(a) Stress-strain profile of the section (b) Schematic load-deflection curve

Figure. A.1. Sectional analysis of strengthened beam.

From force equilibrium, the forces C, T_s, and T_{NSM} can be expressed in the following manner:

$$C = \lambda x.b.f_c' \quad \text{(B.1)}$$

$$T_s = A_s.f_y \quad \text{(B.2)}$$

$$T_{NSM} = A_f.E_f.\varepsilon_f \quad \text{(B.3)}$$

The moment-curvature distribution of the beam can be divided into three stages as follows:

Pre-cracked stage: $0 \leq M_a \leq M_{cr}$

The cracking moment of the strengthened concrete beam, M_{cr}, is considered as similar to that of a non-strengthened beam by taking the tensile concrete strength into account:

$$M_a = \frac{f_t I_0}{h - x_0} \quad \text{(B.4)}$$

The moment of inertia of the uncracked section, I_0, can be expressed as:

$$I_0 = \frac{bx_0^3}{3} + \frac{b(h-x_0)^3}{3} + nA_s(d_s - x_0)^2 + n_f A_f \left(d_f - x_0\right)^2 \quad \text{(B.5)}$$

and

$$x_0 = \frac{\frac{bh^2}{2} + nA_s d_s + n_f A_f d_f}{bh + nA_s + n_f A_f} \quad \text{(B.6)}$$

where n = E_s/E_c and $n_f = E_f/E_c$. In the above equations, b = beam width; h = beam height, A_s = steel cross-sectional area; d_s and d_f are the distances between the most compressed concrete fibre and the centre of gravity of the steel bars and the CFRP rods/strips, respectively; x_0 = distance between the most compressed concrete fibre and the neutral axis before concrete cracking; E_c, E_s, E_f are the elastic modulus of concrete, steel bars and CFRP rods, respectively; and f_t is the concrete tensile strength at 28 days.

Pre-yield stage $M_{cr} \geq M_a \geq M_y$

The bending moment of the strengthened section at the steel yielding level, M_y, is calculated by considering that the strain of the steel reinforcement has reached the yielding strain, according to the following equation:

$$M_y = \frac{nf_y I_c}{d_s - x_0} \quad \text{(B.7)}$$

The moment of inertia of the cracked section, I_c, can be expressed as:

$$I_c = \frac{bx_0^3}{3} + nA_s(d_s - x_0)^2 + n_f A_f \left(d_f - x_0\right)^2 \quad \text{(B.8)}$$

and

$$x_0 = \frac{-\left(nA_s + n_f A_f\right) + \sqrt{\left(nA_s + n_f A_f\right)^2 + 2b\left(nA_s d_s + n_f A_f d_f\right)}}{b} \quad \text{(B.9)}$$

where x_0 is the distance between the most compressed concrete fibre and the neutral axis after concrete cracking

Post-yield stage $M_y \geq M_a \geq M_u$

From Figure A1, the strain developed in the FRP rod/strip (ε_{NSM}) can be calculated as:

$$\varepsilon_f = \varepsilon_c . \frac{d_f - x}{x} \leq \varepsilon_{fu} \quad \text{(B.10)}$$

where ε_f is the strain in the NSM reinforcement; ε_c is the strain of the top fibre of concrete; x is the neutral axis depth; and $\varepsilon_{fu}$is the ultimate strain in the NSM FRP rod/strips. The neutral axis x can be obtained by substituting Equation (B.10) into Equation (B.3), and the ultimate moment of the section M_u can be computed as follows:

$$M_u = A_s f_y (d_s - 0.4x) + A_{NSM} E_{NSM} \varepsilon_c . \left[\frac{d_{NSM} - x}{x}\right] . (d_f - 0.4x) \quad \text{(B.11)}$$

Appendix C: Example of crack patterns and FRP stresses obtained from the FE analyses.

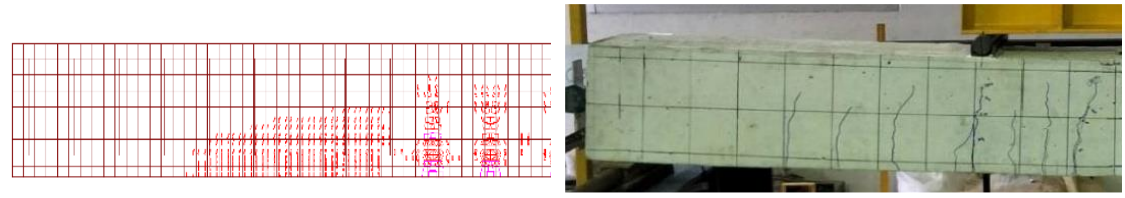

(a) (b)

Figure C1. Comparison of crack patterns for beam TB1 from (a) FE analyses, and b) experiments.

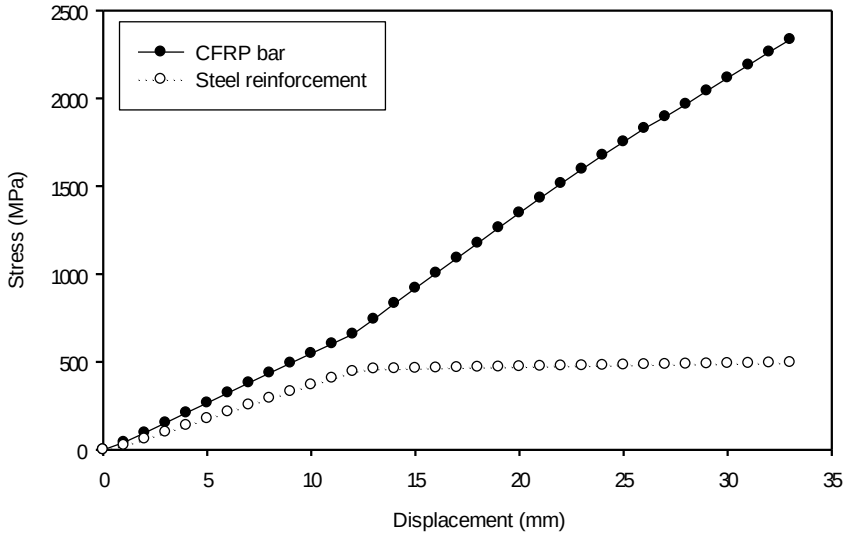

Figure C2. Typical evolution of stresses in the steel bars and CFRP rod during the FE simulation (Beam TB2).